A new and facile co-modification by introducing oxygen vacancies and loading Ag nanoparticles to promote the photocatalytic activities of Bi_2WO_6

Yue Huang[a,*], Xiaoqiang Zhang[a], Zhonghua Zhou[a,*], Shirley Shen[b]

[a] *College of Materials, Xiamen University, Xiamen, Fujian 361005 China*
[b] *CSIRO Manufacturing, Clayton, VIC 3168, Australia*

ARTICLE INFO

ABSTRACT

A new and facile co-modification by introducing oxygen vacancies and loading Ag nanoparticles to largely promote the visible-light-driven photocatalytic activities of Bi_2WO_6 semiconductor photocatalyst has been studied. Bi_2WO_6 (BWO) flower-like micro-spheres were prepared by a hydrothermal method. Oxygen vacancies (OV) were introduced by a hydrogen reduction method and the concentration of OV was controlled by the heat treatment temperature under H_2 atmosphere. After OV modification, Ag nanoparticles were loaded on the BWO micro-sphere surface by a photo-reduction method and the Ag loaded content was controlled by the concentration of $AgNO_3$ solution. Results of visible-light-driven photocatalytic characterizations show that photocatalytic reaction rate constants of OV introduced modified type (BWO@OV) and Ag loaded modified type (BWO@Ag) increase by 1.47 and 1.67 times, respectively, comparing with BWO. Moreover, the reaction rate constant of co-modified type (OV@BWO@Ag) reaches as high as 2.53 times. Introducing OV into BWO enhances the separation of photo-generated electron/hole pairs, and the co-modification by both introducing OV and loading Ag nanoparticles has a synergy promotion effect on photocatalytic activity, which is believed to be a new technical route to enhance semiconductor photocatalytic properties.

1. Introduction

Semiconductor photocatalytic materials and technologies, being able to utilize sunlight, are considered to be ideal technologies for environmental pollution degradation, but still hard to be widely applied due to their low photocatalytic reaction efficiency. The narrow absorbing range of sunlight and the recombination of electron/hole pairs are the key technical bottlenecks needed to be solved [1–7].

Bi_2WO_6 (BWO), a binary metal oxide n-type semiconductor having Aurivillius structure [6], has a narrow bandgap (about 2.8 eV) and is able to absorb visible light, however, its narrow bandgap gives rise to the increase of recombination of photogenerated electrons/holes, leading to its low visible light photocatalytic ability. The studies of restraining electron/hole recombination for BWO are focus on two ways as followings so far. One is to form a heterogeneous structure by combined with wide bandgap semiconductors. For example, a hydrothermal treatment to deposit BWO on TiO_2 nanofiber mat was applied to prepare a 3D BWO/TiO_2 hierarchical hetero-structure formed between the two semiconductors [8]. Due to the valence band (VB) level of BWO is lower, by 0.353 eV, than that of TiO_2, photogenerated holes in the VB of BWO can be transferred to that of TiO_2 and the probability

of electron/hole recombination decreases, which results in enhanced visible photocatalytic degradation performances [8]. Besides, MoS_2 [9], g-C_3N_4 [10], WO_3 [11], ZnO [12] semiconductors were also reported to be combined with BWO to form heterogeneous structures. The second way is to modify BWO by surface loading with high conductivity materials, such as carbon, noble metal nanoparticles. Graphene/BWO [13], C/BWO microsphere [14], Pt/BWO [15,16], Au/BWO [17], Ag/BWO [18] were reported, and the photo-generated electrons in the conduction band (CB) of BWO are transferred to C or noble metal loaded on BWO surface to restrain the electron/hole recombination.

Oxygen vacancies (OV) have two important effects on energy band structure of semiconductor photocatalysts. One is that the existence of OV in crystal lattice of semiconductor induces a shift of VB edge which results in narrowing bandgap and enhancing sunlight harvest capability. For example, OV was introduced into TiO_2 by H_2 reduction treatment to obtain black TiO_2 nanoparticles with a bandgap of only 1.85 eV, the edge of VB shifts from 1.2 eV to −0.3 eV, which results in the band narrowing and the enhanced visible light absorption [19]. Another effect is that the presence of OV creates a new defective energy level below the bottom of CB and induces enhancement of visible light absorption. For example, the OV's state level was reported at 0.75 eV

below CB for H_2 treated TiO_2 nanowire arrays and the visible absorption is attributed to the transitions from the TiO_2 VB to the OV's levels or from the OV's levels to the TiO_2 CB [20]. The effect of OV concentration on the efficiency of perovskite solar cell was also studied by our group by using F-doped TiO_2 nanoparticles as electron transport layer in the cell [21]. For BWO, Kong et al introduced OV into BWO nanoplatelet sample surface by an ethylene glycol-assisted solvothermal approach and realized photocatalytic CO_2 reduction over the full solar spectrum [22]. The effects of OV on restraining the electron/hole recombination and the efficiency of BWO semiconductor photocatalyst are, however, still few reported and an improved understanding is of great interest.

In this work, we have studied a new and facile co-modification to largely promote BWO visible photocatalytic activity by introducing OV into BWO and loading Ag nanoparticles on surface of BWO. Introducing OV into BWO enhances the separation of photo-generated electron/hole pairs, and the co-modification by both introducing OV and loading Ag nanoparticles has a synergy effect on BWO photocatalytic degradation properties, showing a new technical route to promote semiconductor photocatalytic activities.

2. Experimental

2.1. Preparation of Bi_2WO_6 flower-like microspheres

All the chemical reagents used in the experiments were of analytical grade without further purification.

Bi_2WO_6 flower-like micro-spheres (BWO) were prepared by a hydrothermal method referred to [23], using sodium tungstate and bismuth nitrate as raw materials. 1 mmol of sodium tungstate was dissolved in 75 ml deionized water, stirred for 0.5 h to obtain solution A. 2 mmol bismuth nitrate was added to 5 ml 2 mol/L nitrite acid, stirred for 0.5 h to obtain solution B. Then solution B was added to solution A and continued to stir for 1 h to get a mixed solution with white precipitates, which was transferred to a 100 ml Teflon-lined stainless autoclave and heated to 180 ℃ for 24 h. The obtained faint yellow precipitates were filtered and washed several times with deionized water and ethanol, and then dried at 60 ℃ for 6 h.

2.2. Preparation of introducing oxygen vacancy (OV) modified BWO flower-like microspheres (BWO@OV)

Introducing oxygen vacancy modified BWO flower-like microspheres (BWO@OV) have been prepared by a H_2 reduction method using the as-prepared BWO flower-like microspheres as raw materials. In a typical process, 0.4 g as-prepared BWO powders were laid on a ceramic ark and set inside a tube furnace. After the air inside the tube was completely substituted by a mixed gas of H_2 5%/Ar 95%, the powder sample was heated to a setting temperature for 2 h under a gas flow 0.2 L/min of the mixed gas (H_2 5%/Ar 95%). The concentration of OV introduced was controlled by the setting temperature (150 ℃, 200 ℃, 250 ℃ and 300 ℃).

2.3. Preparation of loading Ag modified BWO flower-like microspheres (BWO @Ag)

Loading Ag modified Bi_2WO_6 micro-spheres (BWO@Ag) were prepared by using the as-prepared BWO micro-spheres as raw materials and by a photo-reduction method referred to [24]. 0.7 g as-prepared BWO powders were dispersed in 100 ml 1×10^{-4} mol/L $AgNO_3$ solution. After stirred for 0.5 h in dark, the solution was irradiated by a UV-lamp (365 nm, Toshiba BL 20 W) for 0.5 h. The height between solution and lamp was set to be 200 mm. The obtained grey precipitates were filtered and washed several times with deionized water and ethanol, and then dried at 60 ℃ for 6 h.

2.4. Preparation of introducing OV and loading Ag co-modified BWO flower-like microspheres ($OV@Bi_2WO_6@Ag$)

Using the as-prepared BWO microspheres as raw materials, introducing OV and loading Ag co-modified BWO microspheres ($OV@Bi_2WO_6@Ag$) have been prepared by an order processing of first H_2 reduction and then photo-reduction. The setting temperature of H_2 reduction was 200 ℃. The concentration of Ag loaded was controlled by the $AgNO_3$ solution concentrations (0.5×10^{-4}, 1×10^{-4}, 2×10^{-4} and 5×10^{-4} mole/L).

The opposite order processing of first photo-reduction and then H_2 reduction were not used because this processing combination may induce the increase of grain size of loaded Ag nanoparticles during the second processing of the H_2 heated treatment.

2.5. Structure characterizations

Bruker AXS (D8 advance) X-ray diffraction was used to analyze the phase structures. The XRD patterns were collected under the following conditions: irradiated with graphite monochromatic copper λ (Cu, Kα) = 0.154 nm, at 40 kV, 40 mA, over arrange of 5–90 ° with a step of 0.0163° for 0.05 s. Scanning electron microscope (SEM, HitachiSU-70, 5 kV) was used for morphology characterization and transmission electron microscopy (TEM, JEM-2100, 200 KV) was performed to evaluate the grain sizes and morphology structures. X-ray photoelectron spectroscopy (PHI quantum 2000) with Al Kα as X-ray source was applied to measure the chemical state. All the binding energy was calibrated with the C1s peak at 284.8 eV. UV–vis absorption spectra were recorded by a diffuse reflectance spectroscopy (UV–vis DRS, Lambda 750) using a reference of $BaSO_4$. The electron paramagnetic resonance (EPR) investigation was performed by a Bruker EMX-10/12 spectrometer operating at the X-band frequency. The photoluminescence (FL) characterization was conducted by using fluorophotometer (F-7000, Hitachi) with an excited wavelength of 300 nm. The Brunauer-Emmett-Teller (BET) specific surface areas were measured by nitrogen adsorption using a TriStar 3020 analyzer.

2.6. Visible light photocatalytic measurement

Rhodamine B (Rh B) was chosen to be the model contaminate chemical. 30 mg powder sample was dispersed in 60 ml 10 mg L^{-1} Rh B solution. After kept in dark for 1 h to reach adsorption equilibrium, the photocatalytic reaction was started by irradiating the system using a 500 W xenon lamp as the visible light source with a cutoff filter to cut off the light below 400 nm. At a 20 min interval, the concentration of Rh B left in the solution was analyzed by a UV–vis spectrophotometer (Lambda 750) at the characteristic wavelength (λ = 553 nm), from which the degradation yield was calculated. The photocatalytic activity of the samples can be quantitatively evaluated by comparing the apparent reaction rate constants. The photocatalytic oxidation of Rh B is a pseudo-first-order reaction and its kinetics can be expressed as follows: $kt = \ln(C/C_0)$, where k is the apparent reaction rate constant, C_0 and C are the initial concentration and the reaction concentration of Rh B, respectively.

3. Results and discussion

3.1. Structure and morphologies

Fig. 1 shows XRD patterns of the as-prepared 4 samples of BWO, BWO@OV, BWO@Ag and OV@BWO@Ag. The setting temperature of H_2 reduction was 200 ℃ for the BWO@OV and OV@BWO@Ag samples. The setting concentration of $AgNO_3$ solution during photo-reduction was 1×10^{-4} mole/L for the BWO@Ag and OV@BWO@Ag samples.

The XRD diffraction peaks of the 4 samples agree well with Bi_2WO_6 crystal (JCPDS#39-0256) and there are no impurity peaks, confirming
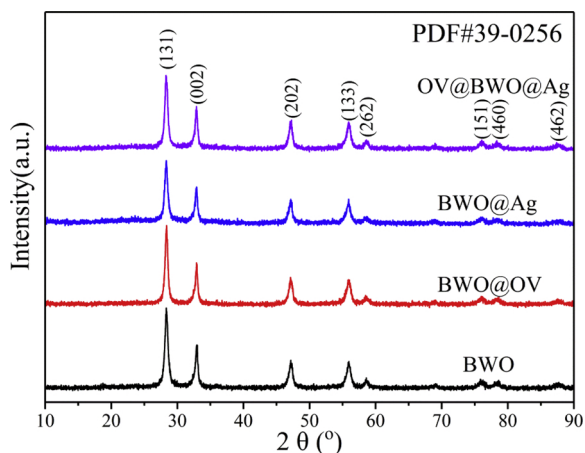
Fig. 1. XRD patterns of Bi_2WO_6 (BWO), introducing OV modified Bi_2WO_6 (BWO@OV), loading Ag modified Bi_2WO_6 (BWO@Ag) and the co-modified Bi_2WO_6 (OV@BWO@Ag).

that all the 4 samples are Bi_2WO_6 crystal. Introducing OV modification, loading Ag modification and the co-modification do not induce the change of the crystal phase. The average grain sizes obtained by the Scherrer equation using the XRD (131) peaks of the 4 samples are 16.11, 17.05, 15.91 and 16.18 nm, respectively. It also confirms that there is no significant change in grain size. For BWO@Ag and OV@BWO@Ag samples, no Ag XRD peaks have been observed due to low crystallinity or amorphous state of loaded Ag nanoparticles [24].

Fig. 2(a–c) shows SEM photos of BWO, BWO@OV and OV@BWO@Ag samples, respectively, Fig. 2(d) and the inset are the enlargements of Fig.2(c) for OV@BWO@Ag sample. The SEM of BWO@Ag (not shown) has the same characteristics as that of BWO. The morphologies of the 4 samples of BWO, BWO@OV, BWO@Ag and OV@BWO@Ag are all flower-like microspheres (2~5 μm in diameter), and from the inset in Fig. 2(d), the flower-like microspheres are composed by overlapping of nanoplates, confirming that introducing OV modification, loading Ag modification and the co-modification do not induce the significant change of morphology. The BET specific surface areas of BWO and BWO@OV are $25\,m^2\,g^{-1}$ and $22\,m^2\,g^{-1}$, respectively, also showing no significant difference under introducing OV process by the H_2 heated treatment at 200 ℃ 2 h.
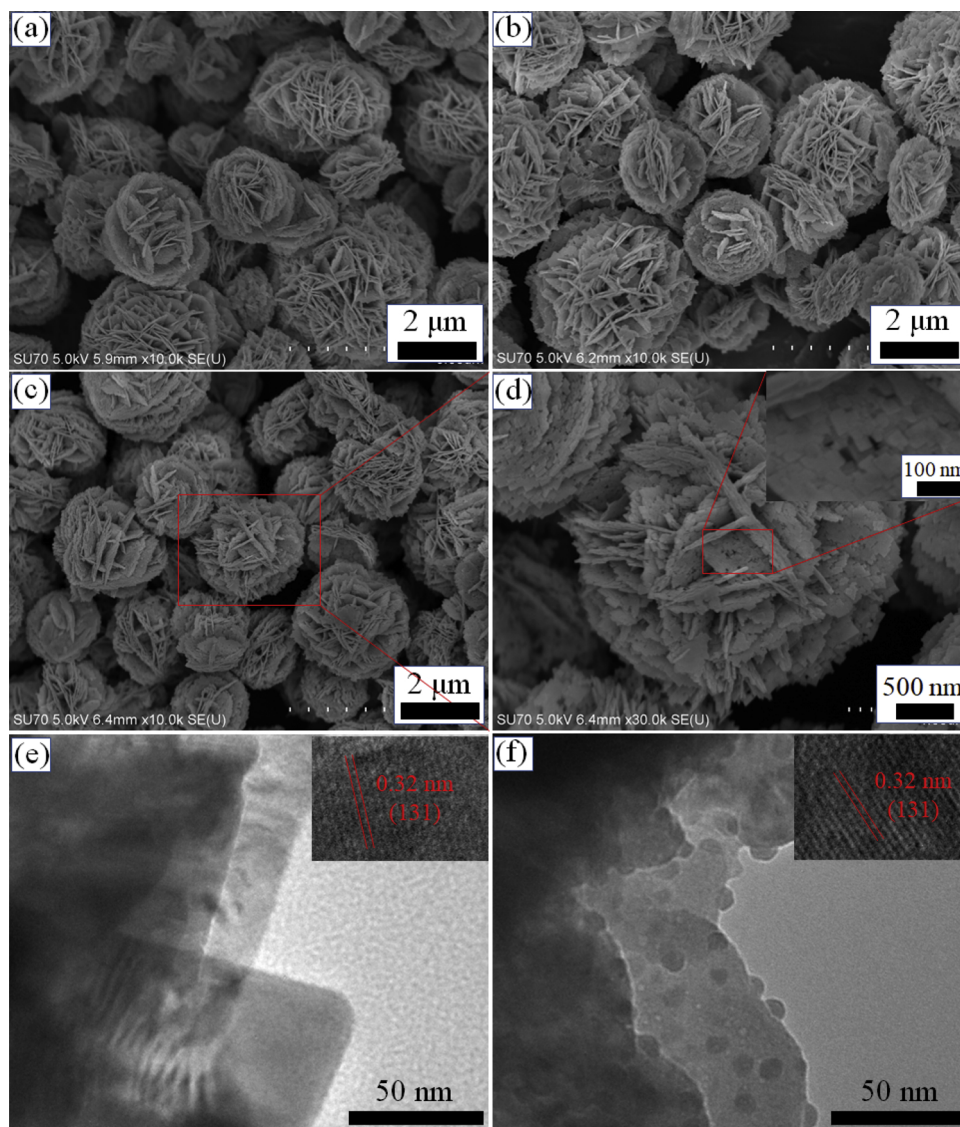

Fig. 2. SEM photos of (a) BWO, (b) BWO@OV and (c) OV@BWO@Ag, (d) and the inset: the enlargement of (c); TEM photos of (e) BWO@OV and (f) OV@BWO@Ag, the insets are the corresponding HRTEM photos.
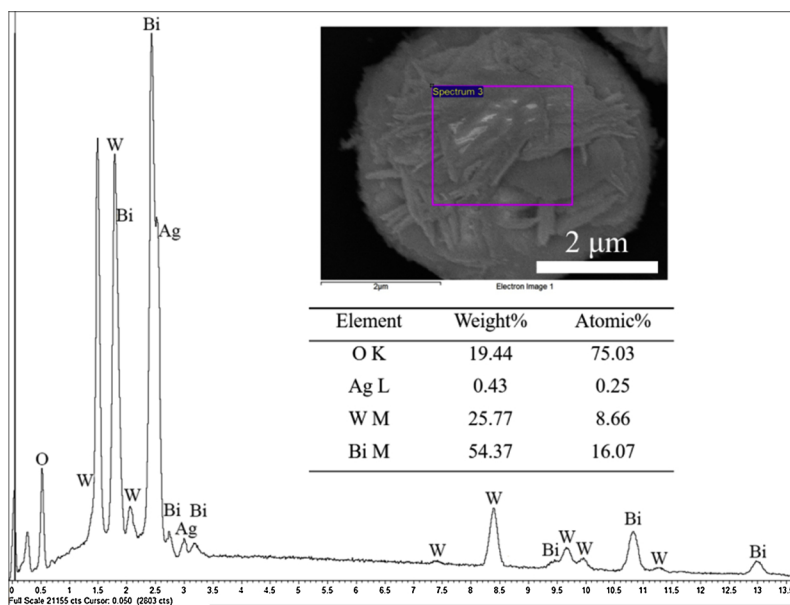
Fig. 3. EDX spectrum and element composition of an OV@BWO@Ag sample.

Loading Ag nanoparticles were confirmed by TEM and EDX characterizations. Fig. 2(e) and (f) show the TEM photos of BWO@OV and OV@BWO@Ag, the insets are the corresponding HRTEM photos. There are no nanoparticles on surface of the nanoplates of BWO@OV sample (Fig. 2(e)), but for OV@BWO@Ag sample (Fig. 2(f)), it can be seen clearly that there are lots of separated nanoparticles (3~5 nm in diameter) loaded on the surface of nanoplates, which are confirmed to be Ag nanoparticles considering the presence of Ag by EDX detection (Fig. 3). The lattice fringe spacings of the two samples are the same to be 0.32 nm (the insets in Fig. 2(e) and (f)), which is corresponding with that of (131) in Bi_2WO_6 crystal (JCPDS#39-0256). It confirms that the nanoplates of BWO@OV and OV@BWO@Ag samples are Bi_2WO_6 crystal and the results agree with those of XRD characterizations (Fig. 1). No lattice fringes were observed on Ag loaded nanoparticles from HRTEM of OV@BWO@Ag, showing that the Ag loaded is amorphous, which agrees with the results of no observation of Ag XRD peaks in XRD characterizations (Fig. 1). Fig. 3 shows EDX spectrum and element composition of the OV@BWO@Ag sample. Only Bi, W, Ag and O elements were detected. Ag concentration is 0.25 atom %. The ratio of Bi (16.07 atom %): W (8.66 atom %) is close to that of Bi_2WO_6 crystal.

3.2. EPR and UV–vis absorption spectra

Fig. 4(a) shows the EPR spectra of the BWO, BWO@OV and OV@BWO@Ag samples. For BWO@OV and OV@BWO@Ag samples, there is a clear EPR peak at g = 1.997, which is attributed to the electrons trapped by OV [25]; while for BWO sample, no EPR peak was observed. For BWO@OV and OV@BWO@Ag samples, OV has been successfully introduced into BWO by the H_2 heated treatment.

Fig. 4(b) shows UV–vis diffuse reflection absorption spectra of the BWO, BWO@OV, BWO@Ag and OV@BWO@Ag samples. Comparing with BWO, the absorption edge of introducing OV sample (BWO@OV) is red-shift, while BWO@Ag and OV@BWO@Ag samples have strong absorption over 450 nm wavelength, which is attributed to localized surface plasmon resonance of loaded Ag nanoparticles [26–28]. The inset in Fig. 4(b) is the plots of $(\alpha h\nu)^2$ vs $h\nu$ (where, α is absorbance, h is Plank's constant, ν is light frequency) [8], and the Eg values of BWO, BWO@OV, BWO@Ag and OV@BWO@Ag samples can be estimated to be 2.97, 2.94, 2.86 and 2.84 eV, respectively.

Fig. 5(a) and (b) are XPS wide scan spectra of BWO and BWO@OV, respectively. For BWO@OV sample, only Bi, W, O and C elements were
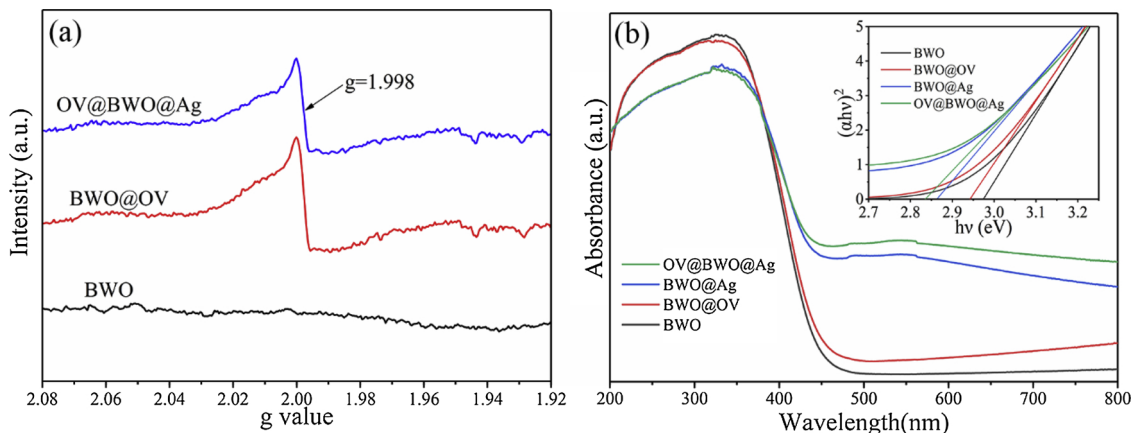

Fig. 4. (a) EPR spectra of BWO, BWO@OV and OV@BWO@Ag; (b) UV–vis diffuse reflection absorption spectra of BWO, BWO@OV, BWO@Ag and OV@BWO@Ag, the inset: the plots of $(\alpha h\nu)^2$ vs $h\nu$.
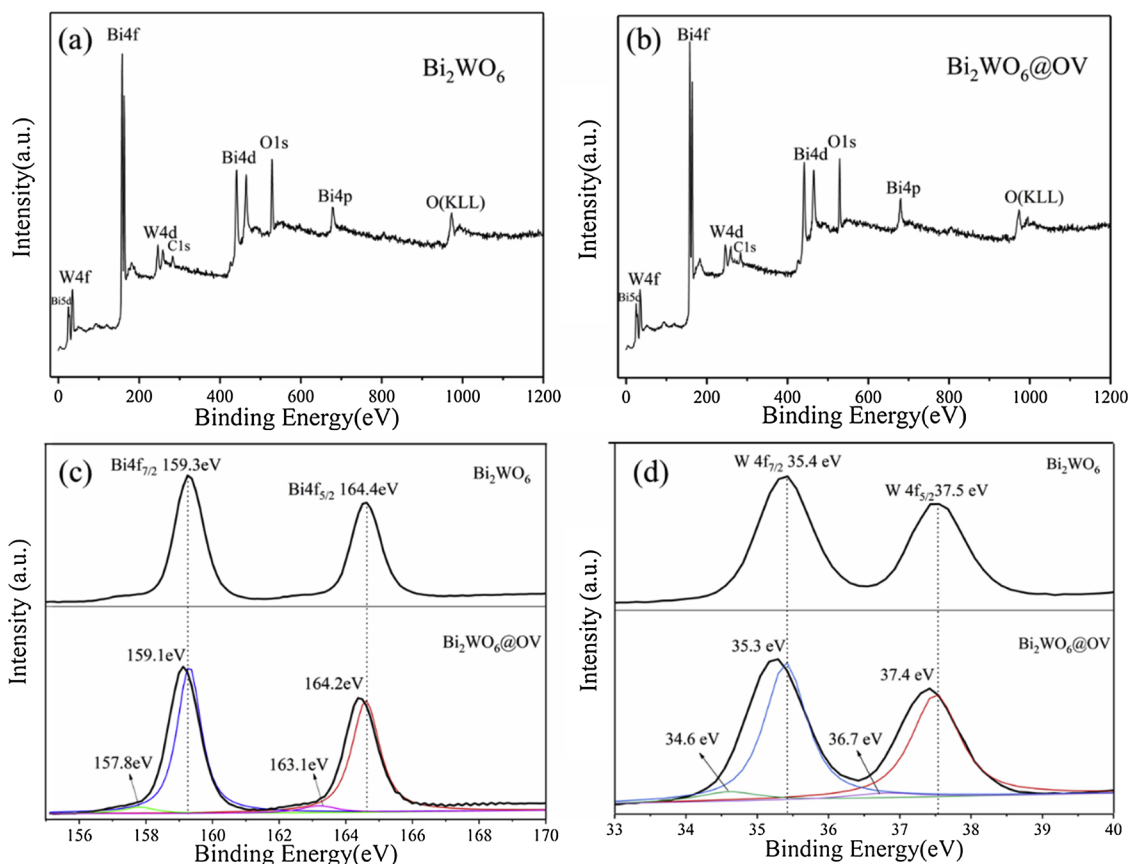
...

Fig. 5. XPS wide spectra of (a) Bi_2WO_6 and (b) $Bi_2WO_6@OV$, and high resolution of (c) Bi4f and (d) W4f of the two samples.

detected (C is the contamination from air and equipment), showing no impurities were involved in the sample during the H_2 heated treatment. Fig. 5(c) shows Bi 4f XPS narrow scan spectra of BWO and BWO@OV, the peaks at 159.3 eV and 164.4 eV are assigned to Bi $4f_{7/2}$ and Bi $4f_{5/2}$ of Bi^{3+} [29]. Comparing with BWO, the peaks of Bi $4f_{7/2}$ and Bi $4f_{5/2}$ of BWO@OV sample have a shift and decrease 0.2 eV. After peak fitting, two peaks at 157.8 eV and 163.1 eV, attributed to Bi^{2+}, were obtained [29].

Fig. 5(d) shows W 4f XPS narrow scan spectra of BWO and BWO@ OV, the peaks at 35.4 eV and 37.5 eV are assigned to W $4f_{7/2}$ and W $4f_{5/2}$ of W^{6+} [30]. Comparing with BWO, the peaks of W $4f_{7/2}$ and W $4f_{5/2}$ of BWO@OV sample also have a shift and decrease 0.1 eV. After peak fitting, two peaks at 34.6 eV and 36.7 eV, attributed to W^{5+}, were obtained [30].

XPS results also confirm that OV has been introduced in BWO@OV

sample, because OV is with positive charges in crystal lattice, and parts of Bi and W elements have to change their chemical valence from Bi^{3+} and W^{6+} states to Bi^{2+} and W^{5+} reduced states for maintaining charge balance.

3.3. Photocatalytic performances

The photocatalytic activities of the 4 samples were measured by photodegradation of Rhodamine B (Rh B) under visible light ($\lambda > 400\,nm$) irradiation. Also, commercial TiO_2 powder (P25, Degussa) was measured for comparison. The Rh B concentration degradation spectra and k values (photocatalytic reaction rate constant) are shown in Fig. 6(a) and (b), respectively. A blank test (Rh B with no catalyst) exhibited little photolysis, and the performance of TiO_2 (P25) is lower than BWO. From Fig. 6(a), after 120 min visible light
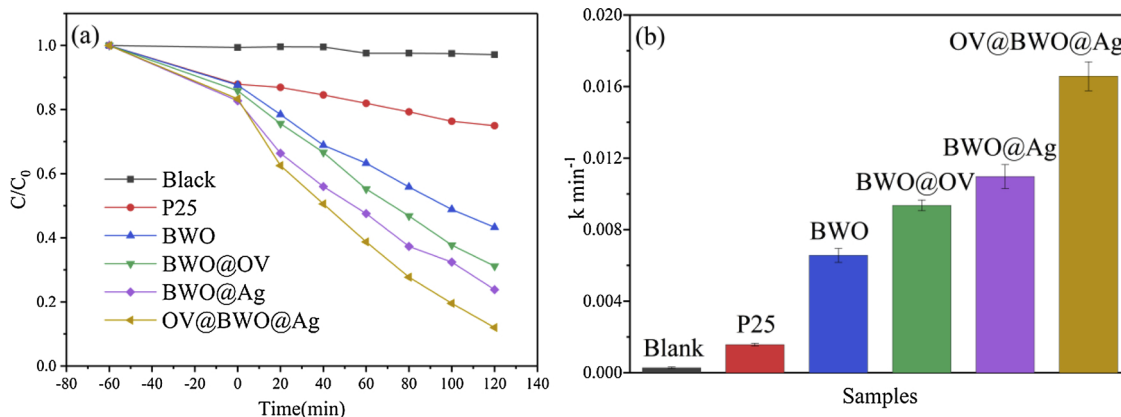

Fig. 6. a) Rh B concentration degradation spectra and (b) reaction rate constant k values. TiO_2 (P25) is for comparison.
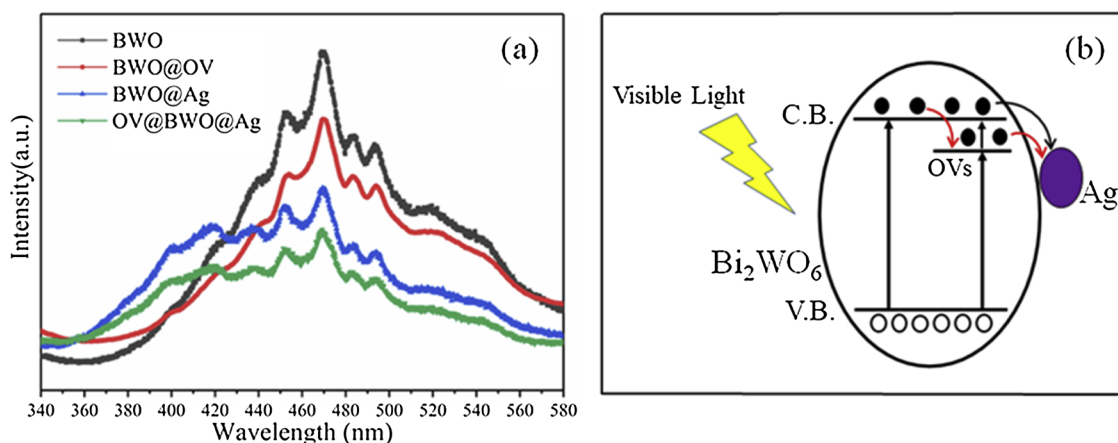
Fig. 7. (a) FL spectra of BWO, BWO@OV, BWO@Ag and OV@BWO@Ag; (b) A schematic diagram of possible mechanism of synergy effects.

irradiation, the values of Rh B degradation efficiency of the 4 samples are OV@BWO@Ag (88%) > BWO@Ag (77%) > BWO@OV (69%) > BWO (57%). Photodegradation reaction of Rh B follows pseudo-first-order kinetics, i.e. kt = ln(C/ C_0), and reaction rate constant k is used to quantitatively characterize photocatalytic activity [18,31]. The k values (Fig. 6(b)) of BWO, BWO@OV, BWO@Ag and OV@BWO@Ag samples are 0.656×10^{-2}, 0.969×10^{-2}, 1.097×10^{-2} and $1.658 \times 10^{-2} \, min^{-1}$, respectively. Comparing with BWO sample, the k values of introducing OV modification (BWO@OV sample) and loading Ag modification (BWO@Ag sample) increase by 1.47 and 1.67 times, respectively. The photocatalytic activities of BWO can be improved by introducing OV modification or loading Ag modification, but the improvement is not significant. However, the k value of co-modification (OV@BWO@Ag sample) increases up to 2.53 times, showing that the co-modification by introducing OV and loading Ag can largely promote the photocatalytic activities of BWO.

On one hand, the effect of OV concentrations on BWO visible photocatalytic activity was conducted by changing H_2 heated temperature (150 ℃ ~ 300 ℃) and confirmed by experiment that 200 ℃ heated temperature is the best. On another hand, the influence of loaded Ag concentrations on BWO visible photocatalytic activity was experimented by controlling $AgNO_3$ solution concentrations (0.5×10^{-4}, 1×10^{-4}, 2×10^{-4} and 5×10^{-4} mol/L), and confirmed that the best Ag loaded concentration is 0.25 atom%. Greater content of Ag loaded hinders the contact of reactants on BWO crystal surface and decreases the photocatalytic activity, agreeing with the results of the reference of [18].

Comparing with single modification of introducing OV or loading Ag nanoparticles, the co-modification by both introducing OV and loading Ag largely promotes the visible photocatalytic activities. Meanwhile, OV@BWO@Ag sample has the lowest FL intensity among the 4 samples (Fig. 7(a)), which indicates that the co-modification sample has the best ability of electron/hole separation. The possible mechanism is shown schematically in Fig. 7(b), ratiocinated by combining with FL characterization results (Fig. 7(a)). OV in crystal lattice can induce OV's energy states under CB [20], while according to that the FL intensity of BWO@OV sample is lower than that of BWO sample (Fig. 7(a)), the introducing OV promotes the separation of photogenerated electron/hole pairs, therefore, it is reasonable to consider that OV's states can trap the electrons excited from VB of BWO and also can trap the photogenerated electrons transferred from CB of BWO. In the case of co-modification of both introducing OV and loading Ag, the photogenerated electrons on the CB of BWO, under the effect of Schottky barrier, are transferred from CB to Ag loaded nanoparticles by two ways: one way is directly through BWO crystal surface, and another way is indirectly, i.e., electrons on CB are transferred first from CB to OV's states inside crystal lattice, then transferred from OV's states to Ag

loaded nanoparticles (shown by the red arrows in Fig. 7(b)), resulting in the best ability of separation of electron/hole pairs among the 4 samples and large promotion of photocatalytic activities. The co-modification by introducing OV and loading Ag has synergy effects to promote the BWO's photocatalytic activities. Further research is expected on the details of OV's states and electron transferring mechanism in the BWO crystal lattice.

4. Conclusion

A new and facile co-modification has been developed by introducing oxygen vacancies and loading Ag nanoparticles to largely enhance the visible light photocatalytic properties of Bi_2WO_6. Comparing with single modification of introducing oxygen vacancies or loading Ag, the co-modification can largely increase the photocatalytic activities. Introducing oxygen vacancies increases the separation of electron/hole pairs, and has a synergy effect on semiconductor photocatalytic properties by combining with loading Ag nanoparticles, showing a new technical route to promote semiconductor photocatalytic activities.

References

[1] M. Nasr, C. Eid, R. Habchi, P. Miele, M. Bechelany, Recent progress on titanium dioxide nanomaterials for photocatalytic applications, ChemSusChem 11 (2018) 3023–3047.
[2] Y. Abdel-Maksoud, E. Imam, A. Ramadan, TiO_2 solar photocatalytic reactor systems: selection of reactor design for scale-up and commercialization-analytical review, Catalysts 6 (2016) 138–163.
[3] S. Ahmed, M.G. Rasul, R. Brown, M.A. Hashib, Influence of parameters on the heterogeneous photocatalytic degradation of pesticides and phenolic contaminants in wastewater: a short review, J. Environ. Manage. 92 (2011) 311–330.
[4] U.G. Akpan, B.H. Hameed, Parameters affecting the photocatalytic degradation of dyes using TiO_2-based photocatalysts: a review, J. Hazard. Mater. 170 (2009) 520–529.
[5] K.K. Paul, P.K. Giri, Shape tailored TiO_2 nanostructures and their hybrids for advanced energy and environmental applications: a review, J. Nanosci. Nanotech. 19 (2019) 307–331.
[6] L.Q. Jing, W. Zhou, G.H. Tian, H.G. Fu, Surface tuning for oxide-based nanomaterials as efficient photocatalysts, Chem. Soc. Rev. 42 (2013) 9509–9549.
[7] Z. Jiao, Y. Tang, P.D. Zhao, et al., Synthesis of Z-scheme g-C_3N_4/PPy/Bi_2WO_6 composite with enhanced visible-light photocatalytic performance, Mater. Res. Bull. 113 (2019) 241–249.
[8] M. Shang, W. Wang, L. Zhang, et al., 3D Bi_2WO_6/TiO_2 hierarchical heterostructure: controllable synthesis and enhanced visible photocatalytic degradation performances, J. Phys. Chem. C 113 (2009) 14727–14731.
[9] J. Zhang, L.H. Huang, H.Y. Jin, et al., Constructing two-dimension MoS_2/Bi_2WO_6

core-shell heterostructure as carriers transfer channel for enhancing photocatalytic activity, Mater. Res. Bull. 85 (2017) 140–146.

[10] L. Ge, C. Han, J. Liu, et al., Novel visible light-induced g-C_3N_4/Bi_2WO_6 composite photocatalysts for efficient degradation of methyl orange, Appl. Catal. B-environ. 108 (2011) 100–107.

[11] M. Gui, W. Zhang, Y. Chang, et al., One-step hydrothermal preparation strategy for nanostructured WO_3/Bi_2WO_6 heterojunction with high visible light photocatalytic activity, Chem. Eng. J. 197 (2012) 283–288.

[12] X. Liu, Q. Lu, J. Liu, et al., Electrospinning preparation of one-dimensional ZnO/Bi_2WO_6 heterostructured sub-microbelts with excellent photocatalytic performance, J. Alloys. Compd. 662 (2016) 598–606.

[13] Y. Zhou, X. Zhang, Q. Zhang, et al., Role of graphene on the band structure and interfacial interaction of Bi_2WO_6/graphene composites with enhanced photo-catalytic oxidation of NO, J. Mater. Chem. 2 (2014) 16623–16631.

[14] Y. Chen, X. Cao, J. Kuang, et al., The gas-phase photocatalytic mineralization of benzene over visible-light-driven Bi_2WO_6@C microspheres, Catal. Commun. 12 (2010) 247–250.

[15] M. Qamar, R.B. Elsayed, K. Alhooshani, et al., Highly efficient and selective oxi-dation of aromatic alcohols photocatalyzed by nanoporous hierarchical Pt/Bi_2WO_6 in organic solvent-free environment, ACS Appl. Mater. Inter. 7 (2015) 1257–1269.

[16] H. Zheng, P. Niu, Z. Zhao, et al., Carbon quantum dot sensitized Pt@Bi_2WO_6/FTO electrodes for enhanced photoelectro-catalytic activity of methanol oxidation, RSC Adv. 7 (2017) 26943–26951.

[17] J. Yang, X. Wang, Y. Chen, et al., Enhanced photocatalytic activities of visible-light driven green synthesis in water and environmental remediation on Au/Bi_2WO_6 hybrid nanostructures, RSC Adv. 5 (2015) 9771–9782.

[18] D. Wang, G. Xue, Y. Zhen, et al., Monodispersed Ag nanoparticles loaded on the surface of spherical Bi_2WO_6 nanoarchitectures with enhanced photocatalytic ac-tivities, J. Mater. Chem. 22 (2012) 4751–4758.

[19] A. Naldoni, M. Allieta, S. Santangelo, et al., Effect of nature and location of defects on bandgap narrowing in black TiO_2 nanoparticles, J. Am. Chem. Soc. 134 (2012) 7600–7603.

[20] G.M. Wang, H.Y. Wang, Y.C. Ling, Y.C. Tang, X.Y. Yang, R.C. Fitzmorris, C.C. Wang, J.Z. Zhang, Y. Li, Hydrogen-treated TiO_2 nanowire arrays for photoelectrochemical water splitting, Nano Lett. 11 (2011) 3026–3033.

[21] X.Q. Zhang, Y.P. Wu, Y. Huang, Z.H. Zhou, S. Shen, Reduction of oxygen vacancy and enhanced efficiency of perovskite solar cell by doping fluorine into TiO_2, J. Alloys. Compd. 681 (2016) 191–196.

[22] X.Y. Kong, Y.Y. Choo, S.P. Chai, et al., Oxygen vacancy induced Bi_2WO_6 for the realization of photocatalytic CO_2 reduction over the full solar spectrum: from the UV to the NIR region, Chem. Commun. (Camb.) 52 (2016) 14242–14245.

[23] L. Zhang, W. Wang, L. Zhou, et al., Bi_2WO_6 nano-and microstructures: shape control and associated visible-light-driven photocatalytic activities, Small 3 (2007) 1618–1625.

[24] J. Li, Z. Guo, Z. Zhu, Ag/Bi_2WO_6 plasmonic composites with enhanced visible photocatalytic activity, Ceram. Int. 40 (2014) 6495–6501.

[25] H. Li, J. Shi, K. Zhao, et al., Sustainable molecular oxygen activation with oxygen vacancies on the {001} facets of BiOCl nanosheets under solar light, Nanoscale 6 (2014) 14168–14173.

[26] E. Liu, L. Kang, F. Wu, et al., Photocatalytic reduction of CO_2 into methanol over Ag/TiO_2 nanocomposites enhanced by surface plasmon resonance, Plasmonics 9 (2014) 61–70.

[27] W. Zhao, S. Wang, B. Liu, et al., Exciton–plasmon coupling and electromagnetically induced transparency in monolayer semiconductors hybridized with Ag nano-particles, Adv. Mater. 28 (2016) 2709–2715.

[28] C. Clavero, Plasmon-induced hot-electron generation at nanoparticle/metal-oxide interfaces for photovoltaic and photocatalytic devices, Nat. Photon. 8 (2014) 95–103.

[29] X.Y. Kong, W.P.C. Lee, W.J. Ong, S.P. Chai, A.R. Mohamed, Oxygen-deficient BiOBr as a highly stable photocatalyst for efficient CO_2 reduction into renewable carbon-neutral fuels, ChemCatChem 8 (2016) 3074–3081.

[30] Z.P. Nie, D.K. Ma, G.Y. Fang, W. Chen, S.M. Huang, Concave Bi_2WO_6 nanoplates with oxygen vacancies achieving enhanced electrocatalytic oxygen evolution in near-neutral water, J. Mater. Chem. A 4 (2016) 2438–2444.

[31] Y.P. Wu, Z.H. Zhou, Y.F. Tuo, Y. Huang, S. Shen, A novel and facile method to synthesize self-assembled BiOI microrings composed of nanoplatelets, Mater. Lett. 111 (2013) 43–46.